Overview of nonhyperbolicity and unstable dimension variability in the kicked double rotor

Vitor Hugo Alexandrino Fávaro[1], Leonardo Costa de Souza[2], and Ricardo Luiz Viana[1,3]

[1] Universidade Federal do Paraná, Departamento de Física - 81531-980, Curitiba, Paraná, Brazil
vitor.favaro@ufpr.br
[2] Instituto de Física, Universidade de São Paulo - 05315-970, São Paulo, SP, Brasil
leocsouza@usp.br, lnrd.csouza@gmail.com
[3] Universidade Federal do Paraná, CICTI, NCC - Curitiba, Paraná, Brazil
viana@fisica.ufpr.br

Abstract. This work investigates the robustness of statistical and recurrence quantification measures in chaotic systems exhibiting unstable dimension variability (UDV), a strong manifestation of nonhyperbolicity that compromises the shadowability and reliability of individual numerical trajectories. Using the kicked double rotor, a four-dimensional dissipative map that exhibits broad UDV regimes, we analyze the effects of modeling uncertainties introduced through perturbations in the system dynamics. Although individual trajectories become non-shadowable in the presence of UDV, the results show that statistical quantities such as mean energy, variance, skewness, and kurtosis remain remarkably robust under small perturbations over a wide range of control parameter values. We also examine recurrence quantification analysis measures, particularly determinism and laminarity, which likewise exhibit stability against modeling errors. These results reinforce the viability of statistical and recurrence-based approaches for the characterization of nonhyperbolic chaotic dynamics, even in regimes where UDV reaches maximal intensity, and motivate further investigations in hyperchaotic systems.

Keywords: Shadowability · Kicked double rotor · Numerical simulations · Recurrence analysis.

1 Introduction

The modeling of chaotic systems raises a conceptual issue that goes beyond sensitivity to initial conditions. Numerical simulations inevitably introduce errors associated with machine arithmetic and discretization schemes [1]. In chaotic systems, these errors are exponentially amplified [2], leading to the fundamental question of whether numerical trajectories can still represent valid approximations of true trajectories. This problem is addressed through the concept of model shadowability, which concerns whether pseudo-trajectories generated numerically can be shadowed by true trajectories over physically meaningful times [3,4,5].

In hyperbolic systems, shadowability is guaranteed by classical results from dynamical systems theory [6,7], providing robustness against small perturbations. By contrast, nonhyperbolic systems may exhibit near-tangencies between stable and unstable manifolds, causing a finite-time loss of shadowability [8,9,10]. An even more severe situation occurs in the presence of unstable dimension variability (UDV), where unstable periodic orbits embedded in the same chaotic set possess different numbers of unstable directions [11,12,13,14,15,16]. Under these conditions, trajectories alternate between regions with different local instability, and finite-time Lyapunov exponents fluctuate around zero, strongly reducing shadowing times and the reliability of long-term predictions [17,18,19,20,21,22,23].

From a practical perspective, this raises an important question: even if individual chaotic trajectories cannot be reliably predicted for long times, can the statistical and geometric properties of the dynamics still remain robust? Previous studies suggest that, although UDV compromises the shadowability of single trajectories, statistical observables may still provide meaningful physical information [24]. We apply the ideas of weighted Birkhoff averages [45] to characterize the influence of UDV over the statistical quantities of the system. In addition, recurrence-based methods have become important tools for characterizing complex dynamics, since they quantify temporal organization and geometric structures in phase space through recurrence patterns [25,26,27,28,29].

In this chapter, we present a general exposition of these ideas in the context of the kicked double rotor, a widely studied model that exhibits UDV over a broad range of the control parameter [30]. Besides summarizing its main dynamical transitions, including periodic regimes, chaos, interior crisis, UDV, and hyperchaos, we discuss standard UDV diagnostics based on finite-time Lyapunov exponents. We also show that, despite the low predictability of individual trajectories, certain statistical quantities and recurrence-based properties may remain robust under bounded model uncertainties.

2 Nonhyperbolicity and unstable dimension variability

To discuss non-hyperbolicity and UDV, we will use discrete-time maps $\mathbf{x}_{n+1} = \mathbf{F}(\mathbf{x}_n)$, acting on a chaotic invariant set Λ. However, it is worth noting that the same analysis can be extended to continuous-time equations, such as $d\mathbf{x}/dt = \mathbf{f}(\mathbf{x}, t)$, provided they are considered by Poincaré sections.

As highlighted above, the modeling difficulties (in the sense of the models shadowability) are related to the loss of hyperbolicity of a chaotic invariant set, denoted as Λ. In this context, hyperbolicity is associated with the existence of a well-defined and invariant decomposition into stable and unstable directions. More precisely, we say that Λ is hyperbolic for the map $\mathbf{F}$ if, for every $\mathbf{x} \in \Lambda$, the tangent space $\mathbf{T}_\mathbf{x}$ splits into stable and unstable subspaces $E^s_\mathbf{x}$ and $E^u_\mathbf{x}$, satisfying the following properties [12]:

1. The subspaces are invariant under the action of the Jacobian matrix $\mathbf{DF}$:

$$\mathbf{DF}(E^s_\mathbf{x}) = E^s_{\mathbf{F}(\mathbf{x})}, \qquad \mathbf{DF}(E^u_\mathbf{x}) = E^u_{\mathbf{F}(\mathbf{x})}, \tag{1}$$

2. The splitting of the tangent space $\mathbf{T}_{\mathbf{x}} = \mathbf{E}^s_{\mathbf{x}} \oplus \mathbf{E}^u_{\mathbf{x}}$ varies continuously with $\mathbf{x}$.
3. Vectors in the neighborhood of $\mathbf{E}^s_{\mathbf{x}}$ (respectively $\mathbf{E}^u_{\mathbf{x}}$) approach the forward (respectively backward) iterates of $\mathbf{x}$ at a rate λ; that is, there exist constants $C > 0$ and $0 < \lambda < 1$ such that:
   - if $\mathbf{v} \in E^s_{\mathbf{x}}$, then $|\mathbf{DF}^n(\mathbf{x}) \cdot \mathbf{v}| \leq C\lambda^n |\mathbf{v}|$,
   - if $\mathbf{v} \in E^u_{\mathbf{x}}$, then $|\mathbf{DF}^{-n}(\mathbf{x}) \cdot \mathbf{v}| \leq C\lambda^n |\mathbf{v}|$.

Associated with these subspaces, we define, for each $\mathbf{x} \in \Lambda$, the local stable and unstable manifolds as the sets of points whose trajectories converge to the orbit of $\mathbf{x}$, respectively [7,31]:

$$W^s(\mathbf{x}) = \{\mathbf{y} \in \mathbb{R}^m : \mathbf{F}^n(\mathbf{y}) \to \mathbf{x} \text{ as } n \to \infty\}, \tag{2}$$

$$W^u(\mathbf{x}) = \{\mathbf{y} \in \mathbb{R}^m : \mathbf{F}^{-n}(\mathbf{y}) \to \mathbf{x} \text{ as } n \to \infty\}. \tag{3}$$

According to the invariant manifold theorem, the stable manifold $W^s(\mathbf{x})$ is tangent to the stable subspace $E^s_{\mathbf{x}}$, and the unstable manifold $W^u(\mathbf{x})$ is tangent to the unstable subspace $E^u_{\mathbf{x}}$. Afterward, the way these manifolds intersect becomes relevant for the system dynamics. When the stable and unstable manifolds associated with the same point (or periodic orbit) intersect transversally, we say that there is a homoclinic intersection; if the intersection is nontransversal, there is a homoclinic tangency. Moreover, it is important to emphasize that hyperbolic systems do not exhibit homoclinic tangencies, that is, the angle between the stable and unstable manifolds stays bounded away from zero.

These considerations become particularly relevant when analyzing the validity of numerical simulations in chaotic systems. Consider a deterministic system that generates a chaotic orbit $\{\mathbf{x}_n\}_{n=0}^N$ of finite length N, corresponding to its exact solution. However, in a computational simulation, the evolution is affected by truncation and round-off errors, so the numerically generated trajectory does not coincide exactly with the true orbit. For this reason, this trajectory can be interpreted as a δ-pseudo-trajectory $\{\mathbf{p}_n\}_{n=0}^N$, defined by one-step errors bounded by $\delta > 0$:

$$|\mathbf{p}_{n+1} - \mathbf{F}(\mathbf{p}_n)| < \delta, \qquad n = 0, 1, \ldots, N-1. \tag{4}$$

In this context, the pseudo-trajectory represents what is effectively produced by the computer, whereas the orbit $\{\mathbf{x}_n\}$ corresponds to the exact dynamics of the system. Thus, the central question is whether the numerical trajectory constitutes a good physical representation of the true dynamics. The answer depends on whether the pseudo-trajectory can be ε-shadowed by a true trajectory, that is, whether there exists $\varepsilon > 0$ such that the exact orbit remains close to the numerical trajectory over time:

$$|\mathbf{x}_n - \mathbf{p}_n| < \varepsilon, \qquad n = 0, 1, \ldots, N. \tag{5}$$

Based on these definitions, the concept of model shadowing can be formulated more precisely by interpreting the one-step error δ as a measure of model error. In this case, we investigate whether, for a given level of model uncertainty, the

numerical trajectories can still be associated with the true trajectories of the system. According to the Anosov-Bowen shadowing lemma, hyperbolic systems guarantee that, for any $\varepsilon > 0$, there exists a sufficiently small error δ such that every δ-pseudo-trajectory is ε-shadowed by a true trajectory [6,7].

When the system is not fully hyperbolic, the presence of homoclinic tangencies introduces difficulties in shadowing. In such cases, shadowing occurs only over finite times, remaining valid while the trajectory evolves between regions of near tangency, often called glitches. Thus, when a pseudo-trajectory ceases to be shadowed from some time onward, we say that a glitch has occurred. The average time between such events defines the so-called shadowing time τ, which, for quadratic tangencies, scales as [32]:

$$\tau \sim \varepsilon^{-1/2}. \tag{6}$$

An even more severe form of nonhyperbolicity occurs when the system exhibits unstable dimension variability (UDV). In this scenario, the continuous splitting of the tangent space into stable and unstable subspaces is no longer valid because the invariant set Λ contains regions with different numbers of unstable directions [11].

As a consequence, there coexist unstable periodic orbits with different numbers of unstable directions, densely intermingled in phase space. A typical trajectory then alternates between regions with distinct local dynamics, which favor the frequent occurrence of glitches. For this reason, glitches become so frequent that the shadowing time τ may become very short, compromising the reliability of the numerical modeling.

This behavior was first described by Abraham and Smale in 1970 [11], in the context of a map whose chaotic invariant set Λ contains two fixed points, $\mathbf{q}_1$ and $\mathbf{q}_2$. The point $\mathbf{q}_1$ has a single local expanding direction ($\dim E^u_{\mathbf{q}_1} = 1$), whereas $\mathbf{q}_2$ has two ($\dim E^u_{\mathbf{q}_2} = 2$), characterizing $\dim E^u_{\mathbf{q}_1} \neq \dim E^u_{\mathbf{q}_2}$, which describes UDV.

The effect of the different numbers of unstable directions associated with $\mathbf{q}_1$ and $\mathbf{q}_2$ can be quantified through the finite-time Lyapunov exponents n, particularly the one closest to zero. These exponents describe the average rates of expansion or contraction along the different directions in phase space and, for the j-th direction, are defined as [17,19,20]

$$\tilde{\lambda}_j(\mathbf{x}_0, n) = \frac{1}{n} \ln ||\mathbf{D}\mathbf{F}^n(\mathbf{x}_0) \cdot \mathbf{v}_j||, \quad j = 1, 2, \ldots, m, \tag{7}$$

where $\mathbf{v}_j$ is the singular vector associated with the j-th singular value of the tangent map iterated n times. Notice that Eq. (7) depends explicitly on the initial condition $\mathbf{x}_0$, in contrast to the usual Lyapunov exponent obtained in the infinite-time limit,

$$\lambda_j = \lim_{n\to\infty} \tilde{\lambda}_j(\mathbf{x}_0, n), \tag{8}$$

which is independent of that choice. Consequently, when considering a set of initial conditions, this intrinsic finite-time dependence allows us to describe the

variation of $\tilde{\lambda}_j(\mathbf{x}_0, n)$ statistically, characterizing it through a probability density function (PDF) $P(\tilde{\lambda}_j(\mathbf{x}_0, n))$.

From this distribution, it is possible to compute its statistical moments. For example, we can define the mean as [17,18,19]

$$m_j(n) = \langle \tilde{\lambda}_j(\mathbf{x}_0, n) \rangle = \int_{-\infty}^{\infty} \tilde{\lambda}_j(\mathbf{x}_0, n)\, P(\tilde{\lambda}_j(\mathbf{x}_0, n))\, d\tilde{\lambda}_j(\mathbf{x}_0, n), \tag{9}$$

and, consequently, the variance is given by

$$\begin{aligned} \sigma_j^2(n) &= \left\langle \Big(\tilde{\lambda}_j(\mathbf{x}_0, n) - m_j(n) \Big)^2 \right\rangle \\ &= \int_{-\infty}^{\infty} \Big(\tilde{\lambda}_j(\mathbf{x}_0, n) - m_j(n) \Big)^2 \, P(\tilde{\lambda}_j(\mathbf{x}_0, n))\, d\tilde{\lambda}_j(\mathbf{x}_0, n). \end{aligned} \tag{10}$$

In addition, we can define the fraction of finite-time Lyapunov exponents that take positive values as [18]:

$$\phi_j(n) = \int_0^{\infty} P(\tilde{\lambda}_j(\mathbf{x}_0, n)) d\tilde{\lambda}_j(\mathbf{x}_0, n). \tag{11}$$

Since Eq. (11) measures the relative frequency of positive exponents along the trajectory, values of $\phi_j(n)$ between 0 and 1 indicate the coexistence of positive and negative exponents, which characterizes the presence of UDV. Moreover, if $\phi_j(n) \approx 1/2$, positive and negative exponents occur with equal frequency, corresponding to a regime in which UDV is maximal [21]. In that case, the mean tends toward values close to zero.

Returning to the Abraham-Smale example, we consider the second largest finite-time Lyapunov exponent $\tilde{\lambda}_2(\mathbf{x}_0, n)$, since it is the one closest to zero [19]. In trajectories with UDV, this exponent takes positive values when the orbit remains near $\mathbf{q}_2$ and negative values when it approaches $\mathbf{q}_1$, reflecting the alternation between regions with different numbers of unstable directions.

As a consequence, $\tilde{\lambda}_2(\mathbf{x}_0, n)$ fluctuates around zero, due to UDV itself, and is directly associated with the occurrence of glitches. In this scenario, the frequent sign changes of $\tilde{\lambda}_2(\mathbf{x}_0, n)$ cause these events to occur repeatedly along the trajectory, so that the shadowing time τ, defined as the average interval between glitches, is typically small.

To quantitatively describe this behavior and estimate the shadowing time, we may use a stochastic model for the dynamics of $\tilde{\lambda}(\mathbf{x}_0, n)$ [19]. In this approach, the shadowing distance d along the corresponding direction evolves, after one iteration of the map, as

$$d_{n+1} \sim d_n \exp\big(\tilde{\lambda}(\mathbf{x}_0, 1)\big), \tag{12}$$

so that the logarithmic distance $z = \ln|d|$ satisfy an additive process,

$$z_{n+1} = z_n + \tilde{\lambda}(\mathbf{x}_0, 1). \tag{13}$$

By treating the one-step finite-time Lyapunov exponents $\tilde{\lambda}(\mathbf{x}_0, 1)$ as random variables, the evolution of z becomes analogous to a random walk. In this model, the mean m of the exponents determines the drift of the walk, while the variance σ^2 measures the intensity of the fluctuations, so that $\sigma^2(n) = n\sigma^2$ [10]. In the presence of UDV, the distribution of $\tilde{\lambda}(\mathbf{x}_0, 1)$ includes both positive and negative values; thus, depending on the sign of m, shadowing distances tend, on average, to grow or decrease.

Accordingly, the evolution of the PDF of the logarithmic distances $\mathscr{P}(z, n)$ is governed by the Chapman-Kolmogorov diffusion equation, which in the continuous-time limit takes the form [10]:

$$\frac{\partial \mathscr{P}}{\partial n} = \frac{\sigma^2}{2} \frac{\partial^2 \mathscr{P}}{\partial z^2} + m \frac{\partial \mathscr{P}}{\partial z}. \tag{14}$$

The boundary conditions reflect the fact that large shadowing distances are unlikely, and are given by

$$\mathscr{P}(z \to \infty) = 0, \qquad \left(\frac{\partial \mathscr{P}}{\partial z} \right)_{z \to \infty} = 0. \tag{15}$$

In the stationary regime, defined by $\partial \mathscr{P} / \partial n = 0$, we obtain a time-independent equilibrium distribution:

$$\mathscr{P}_{\text{eq}}(z) = \frac{2m}{\sigma^2} \exp\left(\frac{-2mz}{\sigma^2} \right). \tag{16}$$

In this context, the shadowing of trajectories persists as long as the shadowing distances remain sufficiently small. The glitches, which characterize the loss of shadowing, occur when these distances exceed a characteristic length of the attractor, typically of order one. From this description, one can estimate the average time between consecutive glitches for a small modeling error ε, yielding [22]:

$$\tau \sim \varepsilon^{-2m/\sigma^2}, \tag{17}$$

where m and σ^2 correspond, respectively, to the mean and variance of the finite-time Lyapunov exponents closest to zero. When m approaches zero, the shadowing time becomes very short, indicating that, in practice, pseudo-trajectories are unlikely to remain close to true trajectories for long intervals.

3 Kicked double rotor

The first description of UDV in a physically relevant dynamical system was given by Romeiras and collaborators in 1992 [30], who identified this phenomenon in a kicked double rotor. Subsequently, UDV was observed in several other dynamical systems [18,32,33,34,35]. It is believed to be, in fact, ubiquitous in multidimensional systems, including fluid and plasma models [36]. In this section, we briefly present the mathematical model of the kicked double rotor and review the main results in the literature related to its dynamics and the occurrence of UDV.

The kicked double rotor consists of two rods of negligible mass and lengths ℓ_1 and $2\ell_2$, respectively, free to move in a plane, in the absence of gravity, as illustrated in Fig. 1. Particles of mass $m_2/2$ are attached to the ends of the second rod, while a particle of mass m_1 is fixed at the pivot P_2. The angular positions of the rods are described by the angles θ_1 and θ_2.

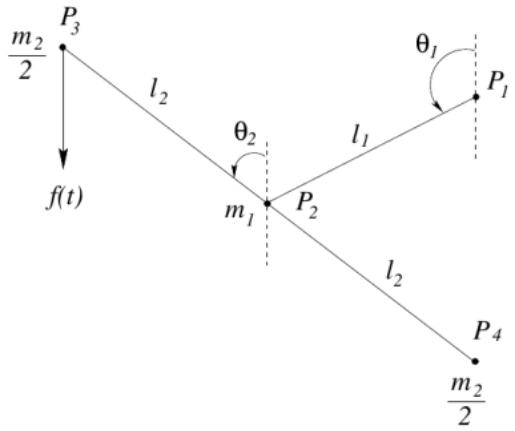


Fig. 1: Schematic representation of the kicked double rotor.

The particle at P_3 is subjected to a periodic impulsive force in time, applied in the vertical direction,

$$f(t) = f_0 \sum_{k=1}^{\infty} \delta(t - kT), \tag{18}$$

where f_0 and T are, respectively, the pulse intensity and the interval between pulses. In addition, there are dissipative effects at the joints P_1 and P_2, represented by viscous forces applied to the rods, proportional to the angular velocities $\dot{\theta}_1$ and $\dot{\theta}_2$, with friction coefficients ν_1 and ν_2.

The equations of motion can be solved analytically between two consecutive pulses and in the neighborhood of a given pulse. Defining the discrete variables $(\theta_{1,2})_n$ and $(\dot{\theta}_{1,2})_n$ as the angular positions and velocities immediately after a pulse at time $t = nT$, one obtains a four-dimensional dissipative map:

$$\mathbf{X}_{n+1} = \mathbf{M}\mathbf{Y}_n + \mathbf{X}_n, \tag{19}$$

$$\mathbf{Y}_{n+1} = \mathbf{L}\mathbf{Y}_n + \mathbf{G}(\mathbf{X}_{n+1}), \tag{20}$$

where we define the vectors

$$\mathbf{X}_n = \begin{pmatrix} (\theta_1)_n \\ (\theta_2)_n \end{pmatrix}, \quad \mathbf{Y}_n = \begin{pmatrix} (\dot{\theta}_1)_n \\ (\dot{\theta}_2)_n \end{pmatrix}, \tag{21}$$

with the angular positions evaluated modulo 2π and the forcing term

$$\mathbf{G}(\mathbf{X}_{n+1}) = f_0 \begin{pmatrix} \frac{1}{\sqrt{2}} \sin(\theta_1)_{n+1} \\ \sin(\theta_2)_{n+1} \end{pmatrix}. \tag{22}$$

For simplicity, we fix the values of all parameters so that $T = m_1 = m_2 = \nu_1 = \nu_2 = \ell_2 = 1$ and $\ell_1 = 1/\sqrt{2}$, leaving the pulse amplitude f_0 as our control parameter. With these choices, the matrices $\mathbf{M}$ and $\mathbf{L}$ are given by:

$$\mathbf{L} = \begin{pmatrix} 0.241427723 & 0.272608937 \\ 0.272608937 & 0.514036661 \end{pmatrix}, \tag{23}$$

$$\mathbf{M} = \begin{pmatrix} 0.485963338 & 0.213354400 \\ 0.213354400 & 0.699317739 \end{pmatrix}. \tag{24}$$

Once the kicked double rotor map has been defined, we analyze the dynamical properties and stability transitions that characterize this system. Due to the symmetry of the equations of motion under the transformations $\mathbf{X} \to -\mathbf{X}$ and $\mathbf{Y} \to -\mathbf{Y}$, the system has an invariant subspace around the fixed point $\mathbf{q}_1 = (0, 0, 0, 0)$. In addition, there is another fixed point, $\mathbf{q}_2 = (\pi, \pi, 0, 0)$, whose stability changes as the control parameter f_0 is varied.

For small values of f_0, the fixed point $\mathbf{q}_2$ is stable. However, when $f_0 = f_1 \approx 4.28$ is reached, it undergoes a period-doubling bifurcation, giving rise to a stable period-2 orbit, which coexists with other periodic and chaotic attractors. This transition can be visualized in the bifurcation diagrams shown in Fig. 2. From this point on, the system exhibits coexistence of periodic and chaotic attractors, a typical behavior of nonlinear systems with multiple stability scales.

As illustrated in the bifurcation diagram for $\dot{\theta}_2$ as a function of f_0 (Fig. 2), increasing the parameter f_0 drives the system through a period-doubling cascade, generating a two-band chaotic attractor at $f_0 = f_2 \approx 6.7469$. Subsequently, these chaotic bands merge into a single chaotic band at $f_0 = f_3 \approx 6.85425$ due to an interior crisis caused by the collision of the two-band attractor with an unstable period-6 orbit. We thus have a pre-crisis attractor A, valid for $f_1 < f_0 < f_3$, and a post-crisis attractor B for $f_0 > f_3$.

The dynamical structure of the pre- and post-crisis attractors was investigated by Kubo *et al.* [21]. By directly computing the eigenvalues of the tangent map $\mathbf{DF}$, they identified saddle-type orbits embedded in A, with unstable dimension $d_u = 1$ and stable dimension $d_s = 3$. For the same interval of f_0, there are also unstable orbits outside A, with $d_u = 2$ and $d_s = 2$. Since these orbits remain outside A before the crisis at $f_0 = f_3$, they are engulfed by the post-crisis attractor B, becoming part of it. This behavior characterizes UDV, since the post-crisis attractor contains orbits with $d_u = 1$ and $d_u = 2$. Based on this analysis, we can state that the onset of UDV occurs at f_3.

To complement the bifurcation analysis, we examine the Lyapunov spectrum. The calculation was performed using 500 random initial conditions, with $0 \leq \theta_{1,2} \leq 2\pi$ and $\dot{\theta}_{1,2} = 0$. We carried out 10^5 iterations, discarding the first 4×10^3 as transient. The exponents were then ordered such that $\lambda_1 \geq \lambda_2 \geq \lambda_3 \geq \lambda_4$,

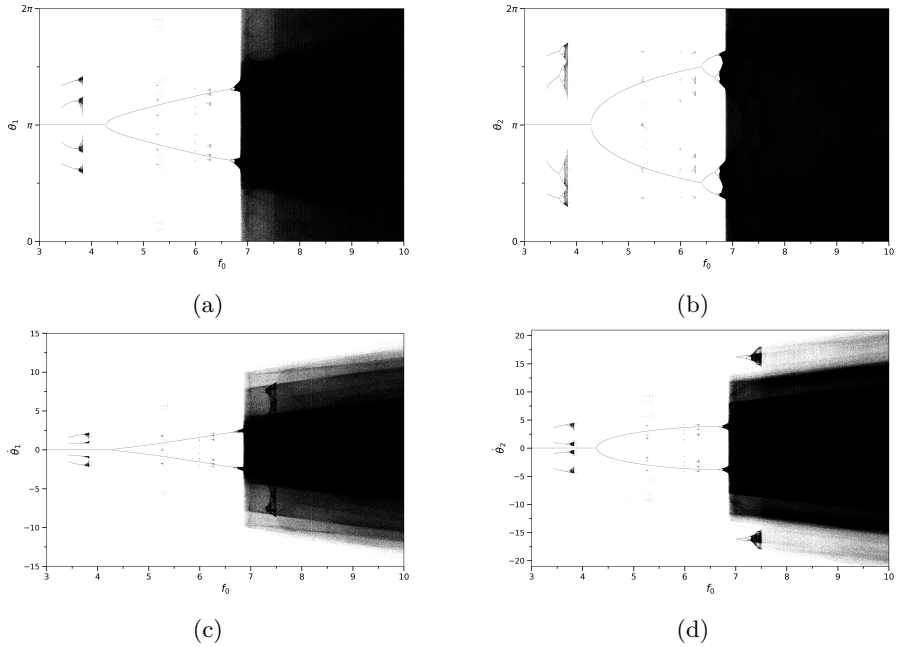


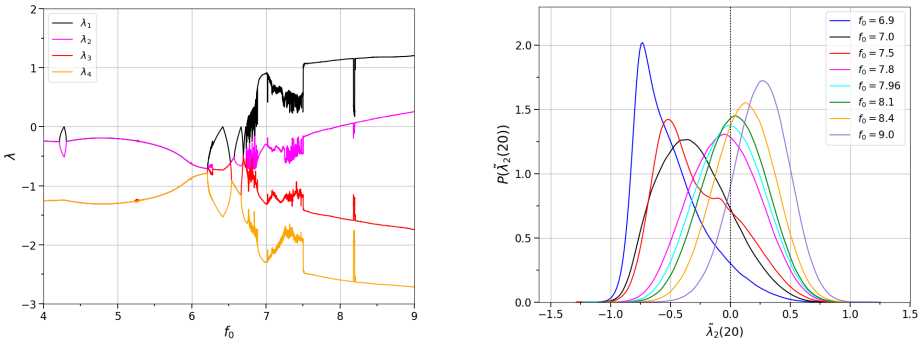
Fig. 2: Bifurcation diagrams for: (a) θ_1 vs. f_0; (b) θ_2 vs. f_0; (c) $\dot{\theta}_1$ vs. f_0; and (d) $\dot{\theta}_2$ vs. f_0.

and plotted as a function of the control parameter f_0, varied in the interval from 0 to 9, with step 10^{-3}. The results are shown in Fig. 3(a).

As illustrated in Fig. 3(a), the first Lyapunov exponent, λ_1, becomes positive at $f_0 = f_2 \approx 6.7469$, indicating the onset of chaotic behavior in the system. As f_0 increases, we observe an interval of intense variation in the four Lyapunov exponents for $f_0 \sim 7.0$–7.5. In addition, we verify that the second exponent, λ_2, also becomes positive at $f_0 = f_4 \approx 7.9632$, characterizing the onset of the hyperchaotic regime. For larger values of f_0, the positive exponents $\lambda_{1,2}$ grow approximately monotonically, while the negative ones $\lambda_{3,4}$ decrease symmetrically.

Once the Lyapunov exponents have been determined, we analyse the one closest to zero, since it is the most relevant for characterizing UDV, as mentioned above. Thus, we computed the finite-time exponent $\tilde{\lambda}_2(n)$ from 1.5×10^5 random initial conditions ($0 \leq \theta_{1,2} \leq 2\pi$ and $\dot{\theta}_{1,2} = 0$). After discarding a transient of 10^4 iterations, the values were obtained after $n = 20$ iterations. The resulting probability distributions for different values of f_0 are shown in Fig. 3(b).

In Fig. 3(b), we show the distributions of $\tilde{\lambda}_2(20)$, they contain positive and negative exponents for all considered values of f_0, indicating that the trajectory visits regions of phase space with different unstable dimensions. For smaller values of f_0, especially below $f_4 \approx 7.96$, the distributions are composed predom-



(a) (b)

Fig. 3: (a) Lyapunov exponents for the kicked double rotor map. (b) Probability distribution of $\tilde{\lambda}_2(20)$ for selected values of the control parameter f_0. Solid lines represent the probability distributions of the exponents, whereas dashed lines correspond to Gaussian fits to the data.

inantly of negative exponents. As f_0 approaches f_4, the distributions become approximately symmetric about zero. For values above this threshold, the dynamics become dominated by positive exponents.

This behavior provides a clear indication of the evolution of UDV with the control parameter. As a complementary measure, we compute the fraction of positive finite-time exponents, $\phi_2(n)$, as defined in Eq. (11). From the numerical standpoint, $\phi_2(20)$ is obtained as the fraction of positive exponents in the computed set for each value of f_0, that is, by the ratio between the number of λ_2 values greater than zero and the total number of exponents. The variation of $\phi_2(20)$ as a function of f_0 is shown in Fig. 4.

It is possible to observe in Fig. 4 that, for small values of f_0, the fraction ϕ_2 is zero, indicating that there is no significant occurrence of positive exponents and, therefore, the system does not exhibit UDV. The appearance of $\phi_2 > 0$ at $f_0 \approx 6.85$ marks the onset of UDV, at which point the attractor begins to contain orbits with different unstable dimensions.

For values of f_0 above this threshold, the fraction ϕ_2 increases gradually, reflecting the growing contribution of locally expanding regions to the dynamics. However, in the interval approximately between $f_0 \sim 7.0$ and 7.5, although $\phi_2(20)$ takes positive values, there is no significant increase in this fraction, with only minor variations occurring. This behavior is also consistent with the Lyapunov exponents λ_j (Fig. 3).

From $f_0 \approx 7.5$ onward, a more pronounced increase in ϕ_2 is observed, indicating that UDV is strengthening. When $f_0 \approx 7.96$, we have $\phi_2 = 0.5$, which means that the system is equally likely to exhibit positive and negative exponents ($m \approx 0$), implying more frequent oscillation between regions with $d_u = 1$ and $d_u = 2$. Under this condition, the shadowing time τ is drastically reduced

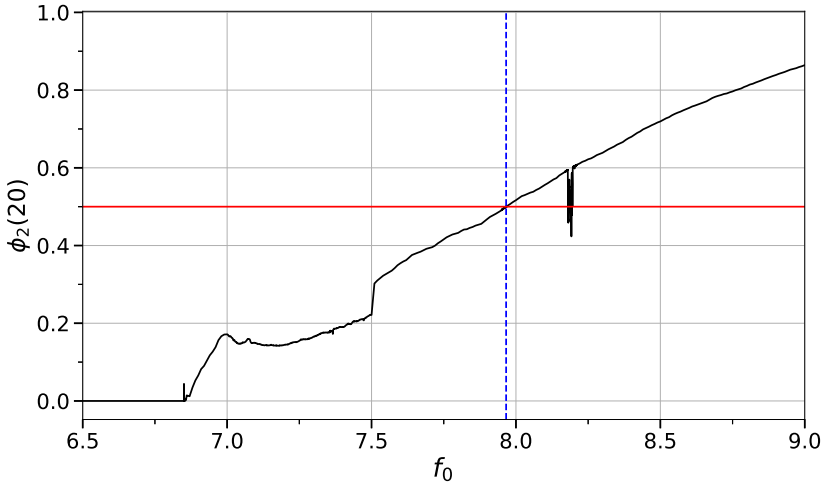


Fig. 4: Fraction of positive finite-time exponents $\phi_2(20)$. The red line represents the value $\phi_2 = 0.5$, while the blue dotted line corresponds to $f_0 \approx 7.96$, at which the UDV intensity is maximal.

($\tau \sim \varepsilon^{-2m/\sigma^2}$), making this scenario the most critical for the reliability of numerical simulations [37].

4 Robustness under bounded model uncertainty

Unstable dimension variability (UDV) undermines shadowability, causing individual numerical trajectories to rapidly lose physical relevance, particularly in parameter regimes where UDV is most severe. Nevertheless, Lai, Grebogi, and Kurths [24] argued that a lack of shadowability does not render all system quantities physically meaningless. While individual trajectories may diverge rapidly, statistical observables derived from trajectory ensembles often remain well-defined and physically relevant [24]. Because these observables are averaged over initial conditions distributed across phase space, reliable system information can still be extracted even without shadowability.

Motivated by this perspective, Lai *et al.* [24] investigated the kicked double rotor subject to modeling error. To simulate numerical errors and model imperfections, they introduced uncertainty via a bounded perturbation applied to the external kicks. Specifically, the system is described by

$$\mathbf{X}_{n+1} = \mathbf{M}\mathbf{Y}_n + \mathbf{X}_n, \tag{25}$$

$$\mathbf{Y}_{n+1} = \mathbf{L}\mathbf{Y}_n + \mathbf{G}(\mathbf{X}_{n+1}) + \varepsilon\,\mathbf{H}(\mathbf{X}_{n+1}), \tag{26}$$

where $\varepsilon \ll f_0$ represents the amplitude of the modeling error and

$$\mathbf{H}(\mathbf{X}_{n+1}) = \begin{pmatrix} \alpha_1 \sin(\theta_1)_{n+1} \\ \alpha_2 \sin(\theta_2)_{n+1} \end{pmatrix}, \tag{27}$$

with α_1 and α_2 being random variables uniformly distributed in the interval $[0, 1]$. This choice ensures a bounded perturbation, preventing the arbitrarily large fluctuations that unbounded distributions (such as Gaussian or Lorentzian) might introduce.

By varying ε over several orders of magnitude, we can systematically simulate different levels of numerical uncertainty and assess the robustness of quantities of interest. This controlled perturbation thus establishes a practical reliability criterion: if specific observables remain insensitive to relatively strong perturbations, they can be regarded as robust and physically meaningful, despite the extreme sensitivity of individual trajectories.

In the present work, we extend the analysis proposed by Lai *et al.* [24], which focused on the specific case $f_0 = 8.0$, to a broader interval of the control parameter f_0. This allow us, to investigate how the robustness of the system properties depends on the dynamical regime, particularly in regions where UDV is intense.

We begin the analysis with the Lyapunov exponents, as an initial probe of the system response to the perturbations. This choice is motivated by the fact that these exponents are typically robust against small modeling variations. The Lyapunov exponents were computed from trajectories with 10^6 iterations, after discarding a transient of 4×10^3 iterations. For each value of the control parameter f_0, averages were performed over 500 random initial conditions uniformly distributed in the interval $0 \leq \theta_{1,2} \leq 2\pi$, with $\dot{\theta}_{1,2} = 0$, in order to reduce statistical fluctuations associated with the choice of initial conditions.

The analyses were carried out for control parameter values in the interval $6.5 \leq f_0 \leq 10$, while the modeling uncertainty was varied over 15 orders of magnitude, from 10^{-1} to 10^{-16}. Fig. 5 presents colormaps of the Lyapunov exponents as functions of the modeling error ε and the control parameter f_0.

In Fig. 5(a), it is possible to observe that, for all values of ε, the onset of the chaotic regime begins at $f_0 \approx 6.75$, since the largest Lyapunov exponent λ_1 becomes positive throughout the entire uncertainty range investigated. In this regime, the dynamics is still dominated by a single unstable direction, while the remaining directions remain contractive.

As f_0 increases toward the range $f_0 \sim 7.0$–7.5, a reorganization of the Lyapunov spectrum is observed, that is, the two largest exponents decrease [Figs. 5(a) and (b)], while the two smallest increase [Figs. 5(c) and (d)]. This redistribution of expansion and contraction rates suggests a qualitative change in the underlying dynamics.

Notably, the Lyapunov exponents remain consistent over several orders of magnitude in the modeling error ε and the control parameter f_0. This result, although expected from a theoretical perspective, is particularly relevant in the context of systems with UDV. Indeed, even in regions of strong nonhyperbolicity, such as near $f_0 = 7.96$, where UDV reaches its maximum intensity, the Lyapunov spectrum remains essentially unchanged under small modeling uncertainties.

However, for stronger perturbations, around $\varepsilon \sim 10^{-2}$–10^{-1}, we observe a slight systematic deviation in the values of the exponents, occurring for all values

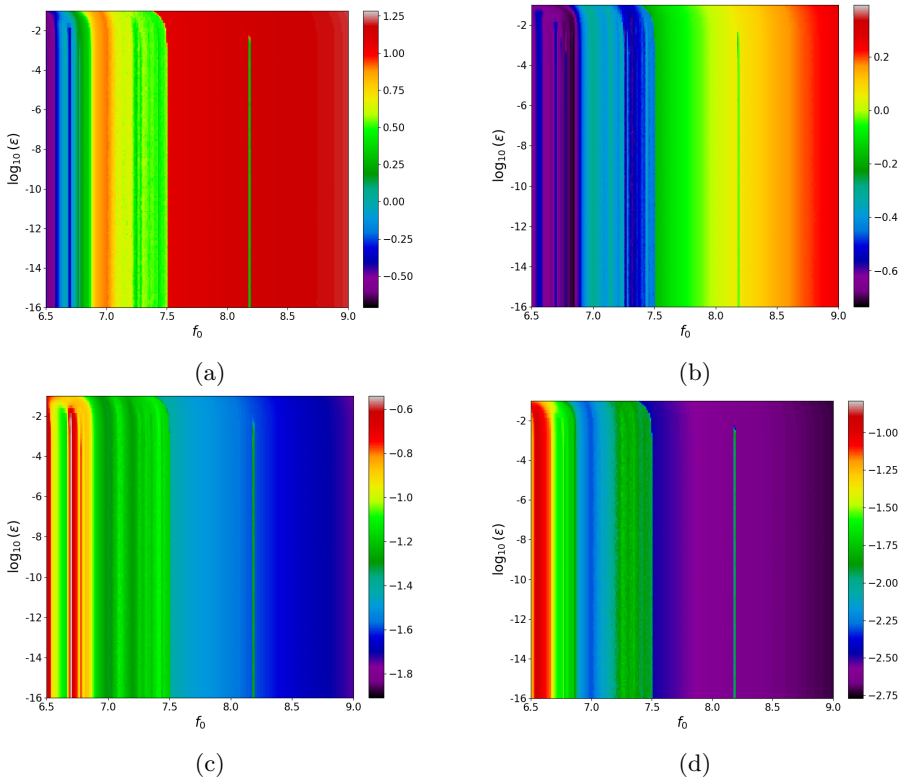


Fig. 5: Colormaps of the Lyapunov exponents: (a) first λ_1; (b) second λ_2; (c) third λ_3; and (d) fourth λ_4, as functions of the modeling error ε and the control parameter f_0.

of f_0, especially in the interval from 6.5 to 7.5. This indicates that, although the Lyapunov exponents are invariant for small uncertainties, their numerical estimates become sensitive once the modeling error is sufficiently large.

Once the robustness of the Lyapunov exponents under small perturbations has been established, we investigate whether the same property is reflected in statistical observables, such as the mean energy and its moments. In this context, for a fixed value of the modeling error ε, we compute quantities of interest, such as the mean system energy $\langle E \rangle$ at a given discrete instant n, in order to characterize the impact of modeling uncertainties on the system energy.

The mean energy of the kicked double rotor map, as proposed by Lai [24], is defined as

$$\langle E \rangle = \lim_{N\to\infty} \frac{1}{N} \sum_{n=1}^{N} \left[\frac{1}{2} \left((\dot{\theta}_1)_n^2 + (\dot{\theta}_2)_n^2 \right) + \frac{1}{\sqrt{2}} \left(\cos(\theta_1)_n + \cos(\theta_2)_n \right) \right], \qquad (28)$$

and, analogously, we also compute the variance, skewness, and kurtosis of the energy, statistical moments that allow a more detailed characterization of the energy distribution over time.

To analyze the behavior of the mean energy $\langle E \rangle$ and the other statistical moments, we developed a program in the `Julia` programming language, varying the control parameter f_0 in the interval from 6.5 to 10 with step size 10^{-3}. For each value, trajectories with $n = 10^8$ points were considered, discarding the first 10^7 as transient. Whereas the work of Lai and collaborators [24] focused on the specific case $f_0 = 8.0$, where UDV is most intense, here we extend the analysis to a broader interval of f_0 in order to investigate how modeling errors and variations of the control parameter influence the statistical properties associated with the energy of the kicked double rotor.

The results obtained for the mean energy, variance, skewness, and kurtosis, as functions of f_0 and the modeling uncertainty ε, are presented in Fig. 6. In general, we observe that these quantities exhibit a more pronounced change in the interval $f_0 \sim 7.0$–7.5, suggesting a qualitative modification in the dynamical behavior of the system in this region.

Fig. 6(a) shows that near the chaos threshold ($f_0 \approx 6.75$), the mean energy $\langle E \rangle$ increases only modestly, remaining on the order of ~ 30. In contrast, across the interval $f_0 \sim 7.0$–7.5, the mean energy grows abruptly and reaches values on the order of ~ 150. This behavior suggests that, in this parameter range, the system begins to explore broader regions of phase space, indicating a significant modification in the underlying dynamics.

This interval coincides with pronounced changes in the Lyapunov spectrum (Fig. 3) and in the bifurcation diagram (Fig. 2). In the same region, the two largest Lyapunov exponents decrease while the two smallest increase, pointing to a redistribution of expansion and contraction rates. Taken together, these results suggest that the abrupt energy increase is tied to a statistical reorganization of the dynamical regime.

The behavior of the variance [Fig. 6(b)] exhibits an abrupt decrease in the same region $f_0 \sim 7.0$. Similarly, the skewness and kurtosis maps [Figs. 6(c) and (d)] also indicate a reduction in this interval, reflecting an energy distribution that becomes more symmetric and less dominated by extreme tails. These changes are consistent with a more homogeneous exploration of phase space after the transition.

Remarkably, across virtually the entire parameter range, the mean energy and its higher-order moments remain unchanged while ε varies over 15 orders of magnitude, from 10^{-1} to 10^{-16}. This robustness is observed even at $f_0 = 7.9632$, the point associated with the maximum intensity of UDV, corroborating the idea that ensemble-averaged statistical quantities can remain reliable even when individual trajectories are not. Small deviations appear only for relatively large perturbations and in narrow parameter intervals, likely associated with isolated periodic windows.

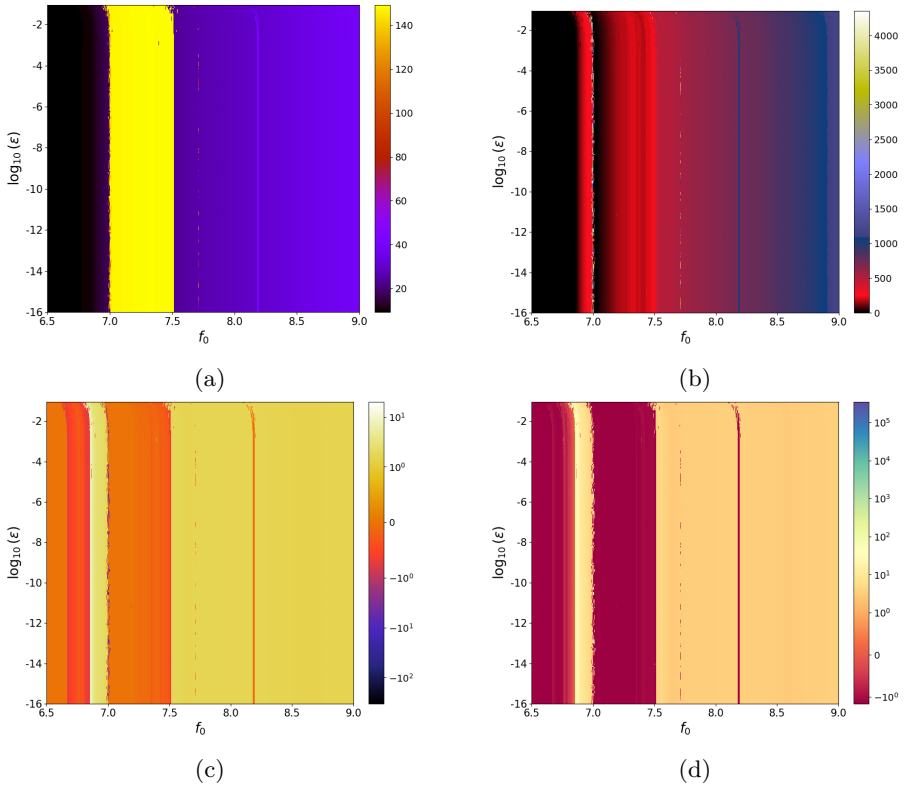


Fig. 6: Colormaps of the (a) mean energy, (b) variance, (c) skewness, and (d) kurtosis, as functions of the modeling error ε and the control parameter f_0.

The time averages of observables are a central tool in the numerical study of chaotic systems. The Birkhoff average of some observable Φ is defined as

$$\hat{\Phi}_N = \frac{1}{N} \sum_{n=0}^{N-1} \Phi(\mathbf{x}_n). \tag{29}$$

This converges to the phase space averages $\langle \Phi \rangle$ for any initial condition if the system is ergodic. According to Birkhoffs Ergodic Theorem, the time average of a continuous observable along a trajectory will converge to its phase space average, provided the system is ergodic. However, in non-hyperbolic systems, the convergence rate of the standard Birkhoff average is heavily bottlenecked by edge effects or boundary sensitive behaviors at the ends of the time series. Das and Yorke [45] proposed a weighted Birkhoff average to circumvent this problem, defined as

$$WB_N(f)(\mathbf{x}_0) = \sum_{n=0}^{N-1} w_{n,N} f \circ \mathbf{M}^n(\mathbf{x}_0), \tag{30}$$

where they define weights

$$w_{n,N} = \frac{g(n/N)}{\sum_{n=0}^{N-1} g(n/N)}, \tag{31}$$

where an exponential bump function

$$g(z) = \begin{cases} \exp\{-[z(1-z)]^{-1}\} & \text{if } 0 < z < 1 \\ 0 & \text{otherwise} \end{cases} \tag{32}$$

was chosen to smooth the behavior at the ends of a finite-time trajectory. This weighting removes the boundary terms that normally limit the convergence of the ordinary average. For regular orbits, the (30) converges superexponentially, faster than any power of $\mathcal{O}(1/N)$, typically reaching machine precision with as few as $10^3 - 10^4$ iterates [46], while for irregular orbits, the convergence remains slow as $\mathcal{O}(1/\sqrt{(N)})$. The difference in convergence rates can be employed to distinguish chaotic and regular orbits of a system if we split a trajectory into two halves and compute the 30 separately for each half; the difference

$$d = -\log_{10} \left| WB_N(f)(\mathbf{x}_0) - WB_N(f)(\mathbf{x}_{N+1}) \right|. \tag{33}$$

For regular orbits, the weighted Birkhoff average converges superexponentially to a unique value. Consequently, the difference between the averages of the two segments rapidly approaches 0 causing the convergence digit d to attain large values (e.g., $d > 8$). Conversely, for chaotic orbits, the local fluctuations in the trajectory cause the difference to diminish at a much slower, power-law rate, resulting in significantly lower values of d over equivalent iteration times N [42,43,41]. In the present work, we apply the weighted Birkhoff averages to the energy,

$$E = \frac{\dot{\theta}_1^2 + \dot{\theta}_2^2}{2} + \frac{\cos\theta_1 + \cos\theta_2}{\sqrt{2}}, \tag{34}$$

using trajectories of the kicked double rotor subject to bounded modeling perturbations. For each combination of the control parameter f_0 and uncertainty amplitude ε, we evolve 100 initial conditions. Each trajectory is first run for a transient of 5×10^4; the subsequent 2×10^5 interactions are divided into two halves of the same length, and the weighted Birkhoff average is accumulated. For this, we use the python package *pynamicalsys* [44]. From the two half averages, we obtain both a robust estimate of the mean energy (we use the average of the two halves) and the convergence digit d, which classifies the regularity of the trajectory. This allows us to compute statistical moments of the energy with reduced bias and, when the orbit is regular, much higher precision than the ordinary average, to separate the contributions of regular and irregular components to the total ensemble; and to monitor how the convergence properties change as the modeling error ε spans over different orders of magnitude.

Fig. 7 summarizes the results of the weighted Birkhoff average of the double rotor. Panel (a) shows the mean kinetic energy $\langle E \rangle$ averaged over 100 random

initial conditions, while panel (b) shows the corresponding mean convergence digit $\langle d \rangle$. For $f_0 \lesssim 6.9$, the mean energy is small and nearly constant across all perturbation levels, and the digit count reaches values of $\langle d \rangle \approx 14$. These regions correspond to periodic windows coexisting with the broader chaotic sea. As the modeling uncertainty increases to intermediate levels ($\varepsilon \sim 10^{-6}$), these periodic windows show remarkable resilience, with their basins of attraction remaining largely intact. However, when the perturbation reaches a macroscopic threshold ($\varepsilon \sim 10^{-2}$), a complete structural transition is observed, the fraction of regular orbits drops to zero, and the mean convergence digit flattens uniformly. This widespread flattening indicates that macroscopic modeling errors induce stochastically driven escapes from the periodic basins, forcing all initial conditions to eventually diffuse into the pervasive chaotic attractor. In panel (c), this is shown more clearly; as the noise increases, the mean digit count decreases, signaling a transition toward more dominant chaotic dynamics.

The mean digit count, Fig. 7(d) displays an exceptionally robust and invariant horizontal morphology. They remain unaltered by changes in the modeling uncertainty across fifteen orders of magnitude, even for the case of the periodic windows.

This invariance demonstrates that while the kicked double rotor operates under non-hyperbolic regimes characterized by severe unstable dimension variability (UDV), its macroscopic statistical profile is remarkably well-behaved. The invariant nature of the chaotic sea's energy profile demonstrates that external modeling noise merely reshuffles the microscopic paths of the trajectories without distorting the underlying ergodic measure of the chaotic attractor.

To complement the statistical analysis, we employ recurrence-based methods, which are widely used to characterize nonlinear dynamical systems. These techniques identify recurrent states in phase space and extract statistical properties from the resulting patterns [27,38].

Let $\mathbf{x}_i = [(\theta_1)_i, (\theta_2)_i, (\dot{\theta}_1)_i, (\dot{\theta}_2)_i]$ denote the state of the system at time i, with $i = 0, 1, 2, \ldots, N$. The recurrence matrix is then defined as

$$R_{i,j} = \Theta(r - |\mathbf{x}_i - \mathbf{x}_j|), \tag{35}$$

where $R_{i,j}$ is a binary matrix that takes the value 1 if the state $\mathbf{x}_j$ lies within a neighborhood of radius r around the state $\mathbf{x}i$, and 0 otherwise [27,28]. Here, $\Theta(x)$ is the Heaviside function, and $|\cdot|$ represents a chosen norm. In this work, we employ the maximum norm [39].

Recurrence plots reveal a variety of dynamical behaviors, and the structures they contain such as vertical and horizontal lines can be quantified. This approach is known as recurrence quantification analysis (RQA). One of the simplest and most fundamental quantifiers is the recurrence rate, which measures the fraction of recurrent points (black pixels in the recurrence plot):

$$RR = \frac{1}{N^2} \sum_{i,j=1}^{N} R_{i,j}, \tag{36}$$

where N is the total number of points in the recurrence plot [26,27].

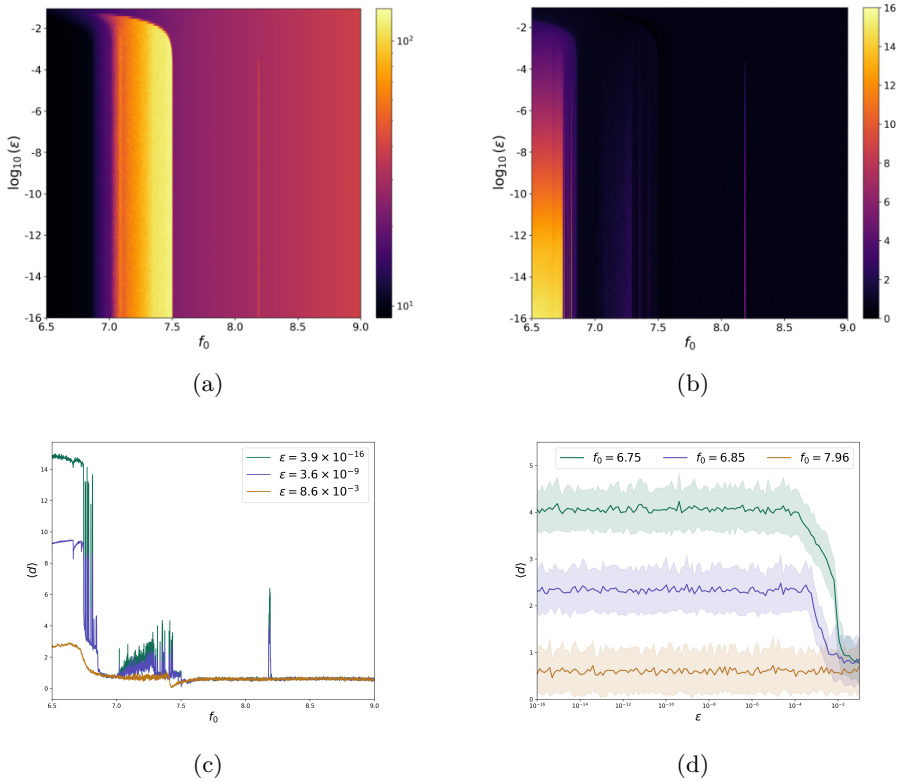


Fig. 7: In (a) colormap of the mean energy, compute from the weighted Birkhoff averages, in (b) colormap of the mean convergence digit. In (c) mean convergence digit $\langle d \rangle$ as a function of forcing amplitude f_0 for three fixed values of ε. In (d) mean convergence digit as a function of modeling error ε for three fixed values of f_0; shaded bands indicate one standard deviation across initial conditions.

Another important structure is diagonal lines, parallel to the identity line $R_{i,i} = 1$ $(i = 1, 2, \ldots, N)$ and defined as

$$R_{i+k,j+k} = 1, \quad (k = 1, 2, \ldots, l), \tag{37}$$

$$R_{i,j} = R_{i+l+1,j+l+1} = 0, \tag{38}$$

where the line begins at (i, j) and end after l successive recurrent points. These lines occur when two segments of the system trajectory evolve similarly for a given period of time and visit the same region of phase space at different times. From these structures, we compute the frequency distribution $P(l)$ of the diagonal line lengths $l_i = 1, 2, \ldots, N_l$, excluding the main diagonal line, which is always present by definition.

In recurrence plots, the presence of many diagonal lines is associated with deterministic behavior. Therefore, a measure used to quantify this feature is the

fraction of points belonging to these structures, known as determinism (DET):

$$DET = \frac{\sum_{l=l_{\min}}^{l_{\max}} lP(l)}{\sum_{l=1}^{l_{\max}} lP(l)}, \tag{39}$$

where $l_{\min}$ and $l_{\max}$ are, respectively, the minimum and maximum lengths of the diagonal lines [27]. It is important to note that the diagonal lengths are related to the inverse of the largest positive Lyapunov exponent of the system.

In addition to diagonal structures, another important feature in recurrence plots is formed by vertical lines, defined as

$$R_{i,j+k} = 1, \quad (k = 1, 2, \ldots, \upsilon), \tag{40}$$

$$R_{i,j} = R_{i,j+\upsilon+1} = 0, \tag{41}$$

where υ is the length of the vertical line. Since the recurrence matrix is symmetric by construction, horizontal lines can be defined analogously to the vertical ones, with essentially equivalent properties. These lines correspond to intervals in which the system state undergoes minimal variations or evolves slowly, reflecting episodes of laminar behavior.

From the frequency distribution of the vertical line lengths $\upsilon_i = 1, 2, \ldots, N_\upsilon$, denoted by $P(\upsilon)$, it is possible to quantify the fraction of points associated with these structures. This fraction is called laminarity (LAM) and is given by

$$LAM = \frac{\sum_{\upsilon=\upsilon_{\min}}^{\upsilon_{\max}} \upsilon P(\upsilon)}{\sum_{\upsilon=1}^{N_\upsilon} \upsilon P(\upsilon)}, \tag{42}$$

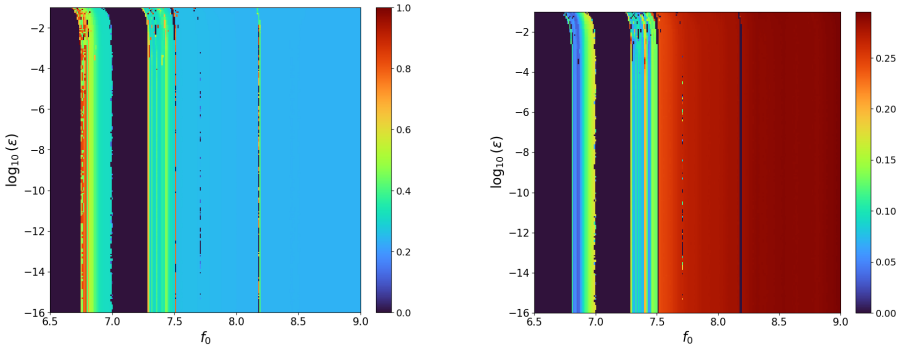
where $\upsilon_{\min}$ and $\upsilon_{\max}$ are, respectively, the minimum and maximum lengths of the vertical lines [27].

Using the recurrence quantification measures described above, we implemented a program in Python employing the `pyunicorn` library to perform the numerical calculations [40]. Following the same methodology used in the statistical analyses [Fig. 6(a)(d)], we computed the determinism and laminarity metrics using Eqs. (25) and (26), varying the control parameter f_0 in the interval 6.5 to 9 with an adaptive step, and varying the model uncertainty ε. Initial conditions were chosen randomly in the interval $0 \leq \theta_{1,2} \leq 2\pi$ with $\dot{\theta}_{1,2} = 0$, and we considered trajectories of $N = 10^8$ points, discarding the first 5×10^7 points as transient.

The recurrence threshold r was chosen such that the recurrence rate was fixed at 10%, meaning that 10% of all pairs of states in phase space are considered recurrent. Smaller values of r reduce the density of points in the recurrence plots, enhancing the detection of subtle dynamical variations, whereas larger values increase this density but reduce the sensitivity to small fluctuations.

From Fig. 8, we verify that determinism and laminarity remain zero up to approximately $f_0 \approx 6.75$–6.8. This behavior is associated with the low imposed value of the recurrence rate ($RR = 10\%$), which causes the recurrence plots to be dominated by isolated points and suppresses the formation of diagonal and vertical structures with minimum length.

In the interval $f_0 \sim 7.0$–7.5, neither determinism nor laminarity is completely suppressed. Around $f_0 \approx 7.3$, both measures increase again, although fluctuations are still observed up to about $f_0 \sim 7.5$. For $f_0 \gtrsim 7.5$, determinism decreases approximately linearly with increasing f_0 [Fig. 8(a)], whereas laminarity increases in the interval $f_0 \sim 7.5$–9.5 and decreases again for $f_0 \gtrsim 9.5$ [Fig. 8(b)].



(a) (b)

Fig. 8: Colormaps of (a) determinism and (b) laminarity as functions of the modeling uncertainty ε and the control parameter f_0.

Despite localized variations for some values of f_0 and ε, neither determinism nor laminarity exhibits a systematic dependence on the modeling uncertainty. Both measures remain essentially unchanged over several orders of magnitude of ε, indicating that the recurrence structure of the system is robust even in the presence of UDV.

Taken together, our results show that the kicked double rotor displays remarkable robustness against bounded modeling uncertainties, even in regimes of strong UDV where individual trajectories rapidly lose shadowability. The Lyapunov exponents, statistical observables, and recurrence quantification measures all remain essentially unaffected by variations of ε over many decades. This persistence of global statistical and recurrence properties confirms that physically meaningful information can still be extracted from the system despite the extreme sensitivity of single trajectories. Our findings thus reinforce the conjecture put forward by Lai *et al.* [24] that ensembletype quantities can remain reliable when shadowability fails. More generally, they indicate that statistical and recurrencebased observables provide robust tools for characterizing nonhyperbolic chaotic systems in the presence of modeling errors.

5 Conclusions

In this work, we investigated the effect of modeling errors in a chaotic system exhibiting unstable dimension variability (UDV), taking the kicked double rotor as the system of study. Motivated by the problem of the reliability of numerical simulations in nonhyperbolic systems, we revisited the work of Lai *et al.* [24] and extended their analysis to a broader interval of the control parameter. In addition, we examined how recurrence-based measures behave under modeling perturbations across this same parameter range.

Our results demonstrate that the lack of shadowability of individual trajectories does not necessarily imply the loss of usefulness of the model for statistical descriptions. In particular, although trajectories in the kicked double rotor become unpredictable due to UDV, statistical information remains stable throughout the investigated parameter interval. This stability indicates that these quantifiers preserve their ability to characterize the system dynamics, even when the individual evolution of trajectories is no longer reliable.

Despite the consistency of the observed results, it is important to emphasize that they were obtained for a specific dynamical system and therefore do not constitute a rigorous proof of general robustness under random bounded perturbations.

As future work, we propose to investigate whether there exists a relationship between unstable dimension variability and the ergodic hypothesis of Statistical Mechanics. We also intend to examine other statistical invariants of dynamical interest, such as fractal dimensions, as well as analyze finite-time statistical and recurrence measures in a manner analogous to what was done for the Lyapunov exponents. In addition, we plan to include an analysis of the natural measure of the system, aiming to evaluate the robustness of these quantities under small random perturbations. Finally, we intend to extend these investigations to continuous flows in order to verify whether the results obtained for discrete maps remain valid in higher-dimensional continuous systems.

Acknowledgments

R.L.V. has been partially supported by the Conselho Nacional de Desenvolvimento Científico e Tecnológico (CNPq, Brazil) under Grants Nos. 403120/2021-7, 443575/2024-0, and 301019/2019-3, and Coordenação de Aperfeiçoamento de Pessoal de Nível Superior (CAPES, Brazil) Grant No. 88881.895032/2023-01. This research is also supported by INCT-NeuroComp (CNPq Grant 408389/2024-9). L.C.S. thanks the São Paulo Research Foundation (FAPESP, Brazil) for financial support under Grant Nos. 2023/16146-6 and 2024/20417-8. V.H.A.F. thanks the Coordenação de Aperfeiçoamento de Pessoal de Nível Superior (CAPES, Brazil) for financial support under Grant No. 88887.954987/2024-00.

References

1. Hairer, E., Nørsett, S. P., Wanner, G.: Solving Ordinary Differential Equations I: Nonstiff Problems. Springer (1993)
2. Lorenz, E. N.: Deterministic Nonperiodic Flow. Journal of the Atmospheric Sciences **20**, 130–141 (1963)
3. Sauer, T., Yorke, J. A.: Rigorous verification of trajectories for the computer simulation of dynamical systems. Nonlinearity **4**(3), 961–979 (1991)
4. Grebogi, C. *et al.*: Shadowing of physical trajectories in chaotic dynamics: Containment and refinement. Physical Review Letters **65**, 1527–1530 (1990)
5. Poon, L. *et al.*: Shadowing in Chaotic Systems. In: Aizawa, Y., Saito, S., Shiraiwa, K. (eds.) Dynamical Systems and Chaos, pp. 13–21. World Scientific, Singapore (1995)
6. Bowen, R.: ω-limit sets for Axiom A diffeomorphisms. Journal of Differential Equations **18**, 333–339 (1975)
7. Viana, R. L. *et al.*: Pseudo-Deterministic Chaotic Systems. International Journal of Bifurcation and Chaos **13**, 3235 (2003)
8. Grebogi, C., Hammel, S., Yorke, J. A.: Do numerical orbits of chaotic dynamical processes represent true orbits? Journal of Complexity **3**(2), 136–145 (1987)
9. Hammel, S., Yorke, J. A., Grebogi, C.: Numerical orbits of chaotic processes represent true orbits? Bulletin of the American Mathematical Society **19**(2), 465–469 (1988)
10. Sauer, T., Grebogi, C., Yorke, J. A.: How Long Do Numerical Chaotic Solutions Remain Valid? Physical Review Letters **79**, 59 (1997)
11. Abraham, R., Smale, S.: Nongenericity of Ω-stability. Proceedings of Symposia in Pure Mathematics **14**, 5 (1970)
12. Guckenheimer, J., Holmes, P.: Nonlinear Oscillations, Dynamical Systems, and Bifurcations of Vector Fields. Applied Mathematical Sciences, vol. 42. Springer-Verlag (1983)
13. Dawson, S. P. *et al.*: Obstructions to Shadowing When a Lyapunov Exponent Fluctuates about Zero. Physical Review Letters **73**, 1927 (1994)
14. Lai, Y.-C.: Unstable dimension variability and complexity in chaotic systems. Physical Review E **59**(4), R3807–R3810 (1999)
15. Saiki, Y., Sanjuán, M. A. F., Yorke, J. A.: Low-dimensional paradigms for high-dimensional hetero-chaos. Chaos **28**, 103110 (2018)
16. Czajkowski, B. M., Viana, R. L.: Periodic orbit description of the blowout bifurcation and riddled basins of chaotic synchronization. Chaos, Solitons & Fractals **184**, 114994 (2024)
17. Kostelich, E. J. *et al.*: Unstable dimension variability: A source of nonhyperbolicity in chaotic systems. Physica D **109**, 81–90 (1997)
18. Viana, R. L., Grebogi, C.: Unstable dimension variability and synchronization of chaotic systems. Physical Review E **62**, 462–468 (2000)
19. Viana, R. L., Pinto, S. E. de S., Grebogi, C.: Chaotic bursting at the onset of unstable dimension variability. Physical Review E **66**, 046213 (2002)
20. Viana, R. L. *et al.*: Simulating a Chaotic Process. Brazilian Journal of Physics **35**, 139 (2005)
21. Kubo, G. T. *et al.*: Crisis-induced unstable dimension variability in a dynamical system. Physics Letters A **372**, 5569 (2008)
22. Do, Y., Lai, Y.-C.: Statistics of shadowing time in nonhyperbolic chaotic systems with unstable dimension variability. Physical Review E **69**(1), 016213 (2004)

23. Sauer, T., Grebogi, C., Yorke, J. A.: Shadowing Lemma and Numerical Computations. Physical Review Letters **79**, 59 (1997)
24. Lai, Y.-C., Grebogi, C., Kurths, J.: Modeling of deterministic chaotic systems. Physical Review E **59**, 2907 (1999)
25. Eckmann, J.-P., Kamphorst, S. O., Ruelle, D.: Recurrence plots of dynamical systems. Europhysics Letters **4**(9), 973–977 (1987)
26. Webber, C. L. Jr., Zbilut, J. P.: Dynamical assessment of physiological systems and states using recurrence plot strategies. Journal of Applied Physiology **76**(2), 965–973 (1994)
27. Marwan, N. *et al.*: Recurrence plots for the analysis of complex systems. Physics Reports **438**(5–6), 237–329 (2007)
28. Marwan, N.: A historical review of recurrence plots. European Physical Journal Special Topics **164**(1), 3–12 (2008)
29. Goswami, B.: A Brief Introduction to Nonlinear Time Series Analysis and Recurrence Plots. Vibration **2**(4), 332–368 (2019)
30. Romeiras, F. J. *et al.*: Controlling chaotic dynamical systems. Physica D **58**, 165 (1992)
31. Lai, Y.-C. *et al.*: Noise-induced unstable dimension variability and transition to chaos in random dynamical systems. Physical Review E **67**(2) (2003)
32. Lai, Y.-C., Grebogi, C.: Modeling of coupled chaotic oscillators. Physical Review Letters **82**, 4803–4806 (1999)
33. Lai, Y.-C. *et al.*: Unstable Dimension Variability in Coupled Chaotic Systems. Physical Review E **60**, 5445–5454 (1999)
34. Barreto, E., So, P.: Mechanisms for the Development of Unstable Dimension Variability and the Breakdown of Shadowing in Coupled Chaotic Systems. Physical Review Letters **85**(12), 2490–2493 (2000)
35. dos Santos, V. *et al.*: Unstable dimension variability structure in the parameter space of coupled Hénon maps. Applied Mathematics and Computation **286**, 23–28 (2016)
36. Galuzio, P. P., Lopes, S. R., Viana, R. L.: Two-state on–off intermittency caused by unstable dimension variability in periodically forced drift waves. Physical Review E **84**(5), 056211 (2011)
37. Sauer, T. D.: Shadowing breakdown and large errors in dynamical simulations of physical systems. Physical Review E **65**, 036220 (2002)
38. Marwan, N. *et al.*: Introduction to focus issue: Recurrence quantification analysis for understanding complex systems. Chaos **28**(8), 085601 (2018)
39. Kraemer, K. H. *et al.*: Recurrence threshold selection for obtaining robust recurrence characteristics in different embedding dimensions. Chaos **28**(8), 085720 (2018)
40. Donges, J. F. *et al.*: Unified functional network and nonlinear time series analysis for complex systems science: The pyunicorn package. Chaos **25**(11), 113101 (2015)
41. Souza, L. C., Mathias, A. C., Caldas, I. L., Elskens, Y., and Viana, R. L. Fractal and Wada escape basins in the chaotic particle drift motion in tokamaks with electrostatic fluctuations. Chaos: An Interdisciplinary Journal of Nonlinear Science, **33**(8) (2023)
42. Sander, E., and Meiss, J. D.: Birkhoff averages and rotational invariant circles for area-preserving maps. Physica D: Nonlinear Phenomena, **411**, 132569 (2020)
43. Sales, M. R., Mugnaine, M., Viana, R. L., Caldas, I. L., and Szezech Jr, J. D. Unpredictability in Hamiltonian systems with a hierarchical phase space. Physics Letters A, **431**, 127991 2022.

44. Sales, M. R., *et al.*: pynamicalsys: A Python toolkit for the analysis of dynamical systems. Chaos, Solitons & Fractals, **201**, 117269 2025
45. Das, S., and Yorke, J. A.: Super convergence of ergodic averages for quasiperiodic orbits. Nonlinearity, **31**(2), 491-501 2018
46. Duignan, N., and Meiss, J. D.: Distinguishing between regular and chaotic orbits of flows by the weighted Birkhoff average. Physica D: Nonlinear Phenomena, **449**, 133749 2023